Pinning mechanism of vortices at antiphase boundaries in $YBa_2Cu_3O_{7-\delta}$

Ch. Jooss
Institut für Materialphysik, Windausweg 2, D-37073 Göttingen, Federal Republic of Germany

R. Warthmann and H. Kronmüller
Max-Planck-Institut für Metallforschung, Heisenbergstraße 1, D-70569 Stuttgart, Federal Republic of Germany
(Received 25 October 1999)

Using quantitative magneto-optics and inversion of Biot-Savart's law for determining critical current density distributions, we investigated the anisotropic vortex pinning at planar defects in $YBa_2Cu_3O_{7-\delta}$ films. Parallel oriented planar antiphase boundaries (APB's) generated in epitaxial thin films grown on vicinal $SrTiO_3$ (001), serve as well defined pinning sites. This array of APB's exerts anisotropic pinning forces on vortex lines which are extraordinary high transverse to the boundary yielding a longitudinal critical current density $j_{c,L}$ up to $\approx 30\%$ of the depairing current parallel to the APB's. Remarkably, also the transverse $j_{c,T}$ crossing the APB's is large for smooth and sharp interfaces corresponding to values usually observed in films on well oriented single-crystalline substrates. Due to variations in the structural width of APB's the magnetic flux penetrating parallel to the defect plane exhibits a filamentary pattern at low fields. It is related to an anomalous low-field dependence of $j_{c,T}$ with a maximum at ≈ 200 mT. In order to distinguish different pinning mechanisms of vortices at planar defects, the angular dependence of the pinning force is calculated approximately and is compared with the experiment. The measured angular and temperature dependence as well as the magnitude of $j_{c,L}$ and $j_{c,T}$ prove that pinning at APB's is dominated by quasiparticle scattering induced variation of condensation energy, characteristic of superconductors with anisotropic order parameter.

I. INTRODUCTION

Generally, in type-II superconductors the critical current is a measure of a volume pinning force exerted to the vortices by defects in the crystal lattice. The largest $j_c \approx (1-3) \times 10^{11}$ A/m^2 at $T=5$ K [$j_c \approx (2-6) \times 10^{10}$ A/m^2 at $T=77$ K] in high-temperature superconductors (HTS's) are usually observed in highly textured epitaxial $YBa_2Cu_3O_{7-\delta}$ (YBCO) films on single-crystalline substrates grown far from thermal equilibrium, e.g., by pulsed laser deposition or sputtering. Due to the complex microstructure with a high density of different lattice defects as well within as between the growth islands, it is very difficult to identify the most effective pinning sites. Correlated disorder in the crystal lattice, such as columnar and planar defects, allows a proper alignment of the vortex system with the defect structure resulting in higher pinning forces compared to collective pinning at pointlike defects[1] Consequently, one-dimensional correlated disorder generated by, e.g., screw dislocations,[2] edge dislocations,[3] dislocation chains,[4] or irradiation induced columnar defects[5] has been attributed to strong pinning of vortices in order to explain the large observed critical current densities.

With respect to island growth related planar defects, highly textured epitaxial YBCO films with large j_c can be imaged as a network of planar defects. For the understanding of the pinning properties of two-dimensional correlated disorder a profound investigation of the transverse critical current $j_{c,T}$ as well as $j_{c,L}$ longitudinal to high current carrying boundaries is essential. In the following, the directions which are transverse and longitudinal to boundaries (both perpendicular to c axis) will be called L and T, respectively. It is already known from twin and antiphase boundaries that planar defects may exhibit a complex and sometimes contradictory behavior with respect to the critical state properties. Twin boundaries (TB's) in single crystals represent strong pinning sites for vortices perpendicular to the boundary.[6,7] On the other hand, TB's may give rise to vortex channeling along the boundary plane[6–9] and reduce $j_{c,T}$. A somewhat different behavior was observed at antiphase boundaries (APB's) in thin films.[10,11] The longitudinal critical current density $j_{c,L}$ in an array of parallel oriented APB's exhibits extraordinary large values up to 30% of the depairing current. Remarkably, at the same time, the transverse $j_{c,T}$ crossing the boundaries reaches the values of $j_{c,T} \approx 1-3 \times 10^{11}$ A/m^2 (5 K) usually being observed in highly textured YBCO epitaxial films on well oriented single-crystalline substrates.[12]

For small-angle grain boundaries (SAGB's), it was shown recently that the dislocation cores represent strong pinning sites for $j_{c,T}$.[13] Simultaneously, it is well known that the critical current density in HTS's is strongly depressed at grain boundaries (GB's) (Ref. 14) which behave fundamentally different compared to GB's in metallic superconductors.[15] The upper limit of the intergranular j_c decreases exponentially with the tilt angle of GB's,[14–16] possibly related to the increasing dislocation content.[17] There is some evidence for charge-carrier depletion at GB dislocations[18] which may result in band bending.[19,20] The weak link behavior for $\theta \geqslant 10-15°$ is attributed to the overlapping of the atomic distortions of dislocation cores at some critical angle θ_c.[21] The observation of strong transverse vortex pinning at boundaries with a very low dislocation content (such as TB's and APB's) indicates that the interface itself represents a strong pinning site for vortices. In view of the strong pinning properties together with the observed rela-

tively large transverse critical currents at APB's,[12] the question arises whether a dislocation free boundary is suppressing superconductivity and, in addition, which interaction mechanism between vortices and such boundaries are dominant and can explain the observed longitudinal and transverse transport properties.

Microscopic theory[22] suggests two fundamentally different mechanisms giving rise to a suppression of the pairing amplitude at GB's in HTS's: (i) a direct weakening of the superconducting condensate by local variations in the coupling constant of the pairs, e.g., due to hole depletion. With respect to pinning of vortices, this effect is usually called δT_c pinning due to the local variation of the transition temperature T_c at the boundary. (ii) An indirect influence of the boundary on the superconducting condensate by scattering of quasiparticles (QP's). This gives rise to a local variation of the QP mean free path l. With respect to pinning this is called δl pinning. In superconductors with isotropic gap the δl effect influences only the kinetic energy of supercurrents. In superconductors with anisotropic gap (e.g., d wave[23]), elastic scattering is able to deplete the condensate (see, for point defects, Ref. 26) and the Anderson theorem[25] is not applicable. Consequently, QP scattering may reduce locally the order parameter similar to the δT_c effect. Different recent work show that the condensate is very sensitive to nonmagnetic scattering and the superconducting charge density n_s is significantly reduced by QP scattering whereas T_c remains more stable.[24,26–28] For large-angle GB's in YBCO the presence of scattering induced localized quasiparticle bound states was proven by tunneling experiments.[29] In contrast to δT_c pinning, where defects of dimensions of at least the coherence length are required for effective pinning, the defect size for QP scattering pinning may be much smaller.[22,30]

Recently, we showed that pinning at growth induced planar APB's with structural width $r_p = 0.7$ nm in YBCO thin films is dominated by quasiparticle scattering induced variation of condensation energy.[12] In this article we extend this study of pinning mechanism at the model system with planar APB's and present measurements on the anisotropic j_c at planar defects with different r_p. This allows an analysis of the factors determining $j_{c,T}$ and $j_{c,L}$. The article is organized as described in the following: Sections II and III give a brief summary of the microstructure of the YBCO films and the experimental techniques. Section IV presents the observed anisotropic current distribution in YBCO films with a nearly perfect array of APB's with $r_p = 0.7$ nm. The dependence of $j_{c,T}$ on r_p is analyzed in Sec. V and Sec. VI gives the magnetic-field dependence of both current components $j_{c,T}$ and $j_{c,L}$. In Sec. VII we present data on the angular dependence of j_c at planar defects and give details of the calculation of the angular pinning force in Sec. VIII. Section IX gives evidence on the length scale of the order-parameter suppression at APB's of different structural width r_p and in Sec. X we derive some conclusions.

II. MICROSTRUCTURE

For the investigation of vortex pinning at planar defects we used two different kinds of YBCO films, both with a high density of parallel oriented antiphase boundaries, but differing in the structural width and smoothness of the APB's. The first kind of YBCO films are grown on almost perfect and stable $SrTiO_3$ (106) surfaces and exhibit a very regular array of APB's with small structural width of $r_p \approx 0.7$ nm. The second kind of films are grown on $SrTiO_3$ surfaces which deviate significantly from the (106) surface. In addition to the APB's, such films exhibit a larger density of APB's with increased distorted region $r_p \approx 2$ nm.

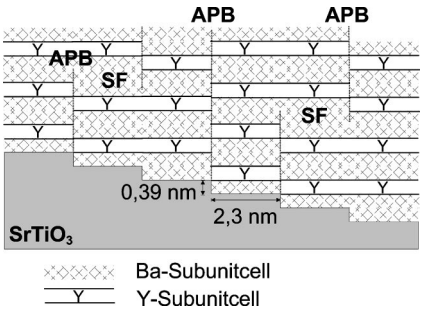

FIG. 1. Schematic drawing of the cross section in T direction of YBCO films on $SrTiO_3$ (106) substrates with the observed microstructure. Due to partial overgrowth the mean distance between APB's perpendicular to the defect plane is three to four times larger than the terrace width of 2.3 nm on the $SrTiO_3$ substrate. The APB's are extended along the c axis over some unit cells of YBCO. They are terminated by the inclusion of a stacking fault (SF) in the (001) plane simultaneously creating a new APB in a region which is shifted some nm in transverse direction.

The $SrTiO_3$ (106) surface is created by cutting $SrTiO_3$ (001) by an angle of 9.46° towards [010] [off (001)]. After UHV annealing at 930 °C, the surface reconstructs in a very regular terrace structure, elongated in [100] direction with 2.3-nm-wide terraces (corresponding to six lattice parameters of $SrTiO_3$ $a_{STO} = 0.39$ nm), separated by steps, mostly a_{STO} high. YBCO films which are deposited by pulsed laser deposition on such substrates are growing by step flow growth mode resulting in a well defined microstructure being dominated by planar APB's. The self-organized defect structure is summarized in Fig. 1 and extensively described in Ref. 11. The planar APB's are oriented parallel to the c axis and have a mean distance of 6 nm transverse (T) to the defect planes (parallel [010]). In longitudinal (L) direction (parallel [100]) the films are very well ordered due to the parallel orientation of the APB planes and the partial suppression of twinning[31] [the b axis of YBCO is mainly (70%) oriented along L]. The width of the APB's $r_p \approx 0.7$ nm is much smaller than the coherence length of YBCO $\xi_{ab} \approx 1.5$ nm. This anisotropic microstructure is well reflected in the mean free path of the charge carriers. Whereas the mean free path in transverse direction $l_T \approx 2-6$ nm corresponds well to the mean distance between planar APB's, the mean free path in longitudinal direction $l_L \approx 70$ nm reaches the values of YBCO single crystals. With this very well defined microstructure YBCO films on $SrTiO_3$ (106) represent an excellent model system for the investigation of vortex pinning and pinning mechanism at planar defects in HTS with a low dislocation density. Related to the termination and creation of APB's by stacking faults, there is a small number of partial dislocations with burgers vector $\mathbf{b} = \frac{1}{3}(0,0,1)$. Since the dislocation lines are oriented parallel [100] they are unfavorable for pinning of vortices $\parallel c$ axis.

Notably, a slight deviation of the miscut angle from

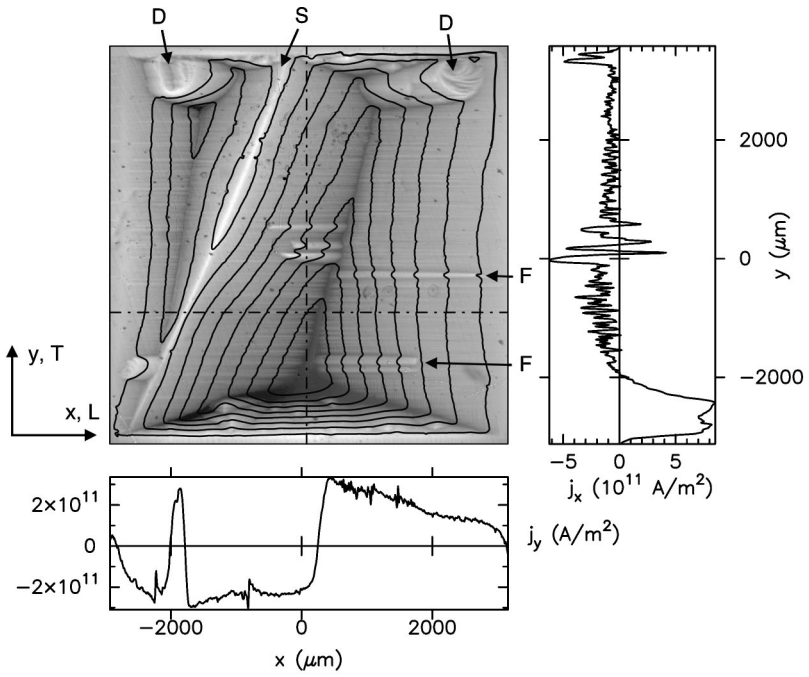

FIG. 2. Magneto-optically observed flux density distribution in a square-shaped, 55-nm-thick YBCO film on $SrTiO_3$ (106) at $B_{ex}=24$ mT and $T=5$ K. The gray scale from black to white corresponds to the perpendicular magnetic flux from zero to the maximum. Full lines are indicating the current path and additionally current density profiles are plotted along the dashed lines.

$\theta_{ideal}=9{,}5°$ as well as a change in the miscut orientation from [010] drastically affects the $SrTiO_3$ surface after UHV annealing. A deviation from θ_{ideal} by $\pm 0.5°$ generates an increasing number of macrosteps of a height of several a_{STO}. In the vicinity of macrosteps on the substrate surface the YBCO films exhibit planar defects similar to APB's but with an extended distorted region $r_p \approx 2$ nm which drastically influence the critical current density. In order to distinguish these APB's with extended r_p from the APB's with small r_p we call them extended defects (ED's). A larger density of ED's due to macrosteps was also observed in YBCO films grown on 9.5° miscut $SrTiO_3$ where the annealing temperature was reduced to 760–800 °C. Moreover, when deviating from the [010] miscut orientation by small angles of 1–5 °, kinks and macro-steps are formed on the surface. We observed that YBCO films on surfaces with a large number of kinks and macro steps are strongly disordered resulting in poor critical current densities.

III. EXPERIMENT

The measurement of the normal magnetic-flux distribution B_z at the surface of all samples was performed by magneto-optical measurements using ferrimagnetic iron garnet indicators with in-plane anisotropy. In one case (Fig. 3) we used EuSe as magneto-optical active layer (MOL) to increase the spatial resolution. The details of the magneto-optical microscope are described in Refs. 32 and 33. The light intensity distribution was measured by means of a charge-coupled device camera (Hamamatsu C4880) with 1000×1018 pixel resolution. The calibration into the magnetic-flux density distribution was done with two different nonlinear calibration functions for both different MOL's. The calibration is described in Ref. 34.

The measurements were done by zero-field cooling (ZFC) the sample and afterwards applying an external field normal to the film plane. For the determination of the current density $\mathbf{j}=(j_x,j_y,0)$ within the film plane, we used an inversion of Biot-Savart's law by convolution theorem. This method is described in detail in Ref. 35. It allows a fast determination of the current-density distribution with a slightly reduced spatial resolution compared to that of the measured B_z due to noise reduction and an accuracy in determining $\mathbf{j}(x,y)$ of $\approx 5\%$.

The magnetization measurements were done by a superconducting quantum interference device (SQUID) magnetometer by zero-field cooling and applying an external field normal to the film plane.

IV. ANISOTROPIC CRITICAL CURRENTS

The flux and current-density distribution of thin square-shaped superconductors with anisotropic critical current was studied theoretically,[36,37] by qualitative experiments[38–42] and quantitative magneto-optics using inversion of Biot-Savart's law.[11,43] Figure 2 shows a quantitative analysis of the current-density distribution superposition of a 55-nm-thick YBCO film grown on perfect $SrTiO_3$ (106). The magneto-optically observed magnetic-flux density distribution is depicted as a gray scale image together with the current streamlines and two profiles of the current densities (corresponding to j_x in Fig. 2) and transverse (j_y) to the APB's.

Due to the anisotropic pinning force of the planar APB's the flux penetrates more easily in L direction than in T direction. This is visible in Fig. 2 although the flux and current-density distribution is drastically different from one observed in a homogeneous YBCO square with anisotropic pinning[11,43,37] (see also, for comparison, Figs. 3 and 5), due to a macroscopic scratch (S), some growth distortions (D), and some other large defects with a diameter of some μm (F). The macroscopic scratch (S) divides the square-sample in two parts which are only weakly connected by the flowing supercurrents. The large defects (F) in the region where the flux penetrates in L direction give rise to large flux filaments which are extended macroscopically towards the center of the sample.

TABLE I. Summary of the properties of different samples with planar APB's (see text). The critical current densities $j_{c,L}$ and $j_{c,T}$ are determined by magneto-optics at $B_{ex}=40$ mT and $T=5$ K. Since $j_{c,T}$ exhibits large variations within a sample due to its strong local-field dependence, we give an average value $\overline{j}_{c,T}$. The anisotropy ratio is defined as $A_j=j_{c,L}/\overline{j}_{c,T}$ and t denotes the thickness of the YBCO films. T_c of all samples is between 89 and 91 K.

Sample	t (nm)	$j_{c,L}$ 10^{11} (A/m^2)	$\overline{j}_{c,T}$ 10^{11} (A/m^2)	$\overline{A}_j$	substrate surface
S1	22	5.5	1.4	3.92	(106)
S2	55	8.5	2.0	4.25	(106)
S3	240	8.0	3.0	2.66	(106)
S4	375	4.1	1.9	2.15	(106)
S5	320	2.7	0.9	3.0	K+MS
S6	155	2.5	0.6	4.2	MS
S7	110	2.2	0.3	7.3	MS
S8	100	1.6	0.5	3.2	K+MS
S9	70	1.0	0.25	4.0	K+MS
S10	180	1.5	0.38	3.9	K+MS
S11	170	3.0	1.0	3.0	IR+MS
S12	150	1.7	0.9	1.9	IR+MS

Despite these effects influencing the pattern of the current, it is clearly visible in the current-density profile, that the magnitude of $j_{c,L}$ flowing in the L direction is exceptionally large up to $j_{c,L}=8.5\times10^{11}$ A/m^2. This is almost 30% of the depairing current density in YBCO of $j_0\approx3\times10^{12}$ A/m^2. Moreover, also the critical current density in T direction $j_{c,T}=2-3\times10^{11}$ A/m^2 is astonishingly large. Although $j_{c,T}$ has to cross the defect planes of the APB's, its magnitude corresponds to the j_c observed in high quality YBCO films on well oriented single-crystalline substrates.

Table I shows the properties of different YBCO films on nearly perfect $SrTiO_3$ (106) (samples S1–S4) as well as on substrates where the miscut angle and miscut direction are deviating $\approx\pm0.5°$ from the values for an ideal (106) surface (samples S5–S10). The substrate surface of samples S6 and S7 exhibits a higher density of macrosteps (MS). Samples S5 and S8–S10 have kinks at the terrace edges of the substrate surface due to a deviation of the miscut from [010] which also leads to the presence of MS. In addition, two samples (S11 and S12) are presented where the 9.5° miscut substrate surface was annealed at 760 °C (instead of 930 °C) and the surface remains more irregular (IR) with a higher density of macrosteps.

Extraordinary large $j_{c,L}$ as well as nice $j_{c,T}$ are reached only for YBCO films on almost perfect (106) surfaces. In case of the samples S5–S8, not only $j_{c,T}$ is reduced to magnitudes below 10^{11} A/m^2 due to the extended distorted region of the ED's. Remarkably, $j_{c,L}$ is also depressed to ordinary values.

V. FLUX FILAMENTS AND LONGITUDINAL PINNING FORCE

In addition to some large flux filaments (F), the flux density in the regions of longitudinal flux penetration in Fig. 2

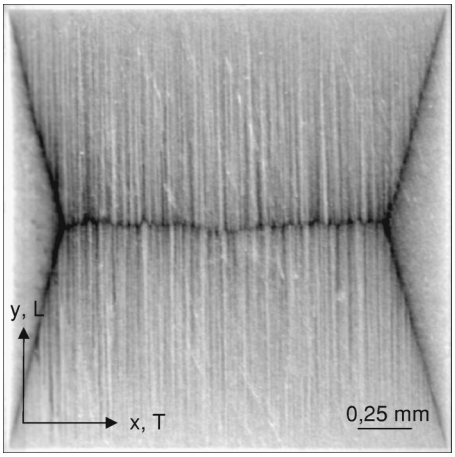

FIG. 3. (a) Flux density distribution of a square-shaped, 170-nm-thick YBCO film (S11) on 9.5° $SrTiO_3$ at $B_{ex}=66.4$ mT and $T=5$ K observed by means of EuSe as magneto-optical layer. The gray scale from black to white corresponds to the perpendicular magnetic flux from zero to the maximum.

exhibits a fine filamentary pattern. The flux filaments are oriented in L direction and extend macroscopically from the film edge towards the center of the sample. The mean distance of the flux filaments in T direction is with $\Delta x\approx60$ μm much larger than the mean distance of APB's. Almost all of the filaments despite those marked with F are extended macroscopically over a size of several mm with origin at those two film edges which are oriented perpendicular to the APB's. Frequently, the filaments which originate from opposite film edges have coincident positions at both flux fronts in the central part of the film. Generally, flux filaments may occur due to two fundamentally different reasons: First, the presence of planar defects with distance Δx where the longitudinal pinning, respectively the transverse critical current density is reduced compared to the area outside the defect plane. From transmission electron microscope (TEM) and scanning tunneling microscope (STM) investigations of the YBCO films we conclude that the filaments are related to the APB's with extended structural width (ED's). Second, large defects with size of some μm where the critical current has to flow around may generate flux filaments in films with anisotropic j_c. The parabolic discontinuity lines extending from such defects towards the sample center due to the bending of the currents are well known from superconductors with isotropic j_c.[35,44] In case of an anisotropic j_c, these parabolas degenerate to a couple of narrow, almost parallel lines[45] which look similar to the filamentary flux pattern at planar weak links, however, are not extended over the entire sample along L. In Fig. 2 almost all flux filaments are related to the ED's despite those which are marked with (F). This is also confirmed by the flux distributions in Figs. 8 and 9 where the filaments are always parallel to the APB's although the angle of the current is changed (see Sec. VII).

The filamentary flux pattern longitudinal to the boundaries is much more clearly visible in Fig. 3. It shows the magnetic-flux distribution of a YBCO film on 9.5° miscut $SrTiO_3$ where the substrate was annealed at a lower temperature $T=760$ °C before depositing the YBCO. This YBCO film exhibits a higher density of ED's and the filamentary flux pattern is more pronounced compared to Fig. 2. The

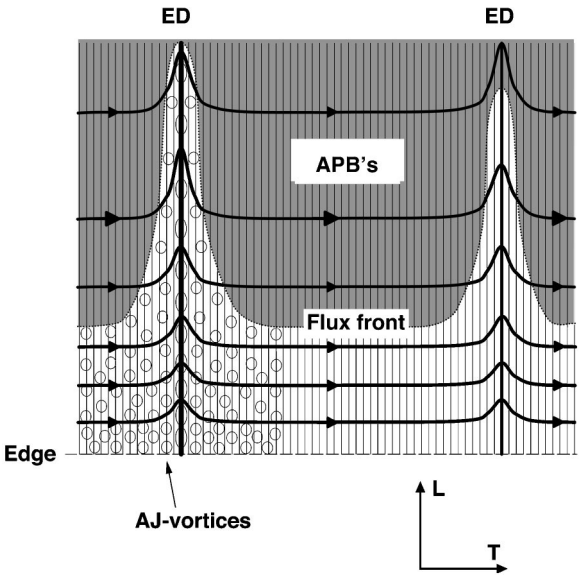

FIG. 4. Sketch of the longitudinal flux penetration in a YBCO film on $SrTiO_3$ (106) with parallel oriented planar defects (APB's). Some of them have a lower longitudinal pinning force (ED's). The density of antiphase boundaries (6 nm) is much larger than indicated in the drawing. The white area is filled by magnetic flux whereas the dark area is still flux free. Ellipses represent Abrikosov-Josephson vortices with different anisotropies.

magneto-optical measurement was performed with EuSe as MOL in order to obtain a higher spatial resolution of 1 μm. The filamentary flux pattern exists only in the area of L penetration of the flux, whereas in the region of T penetration no filamentary structure is visible. The probability that the position of a filament in the upper half of the film in Fig. 3 is corelated to the position of a filament in the lower half is $P=65\%$.

The mean distance between two filaments in T direction in Fig. 3 is $\Delta x=31$ μm which is a factor 2 lower than in the sample on carefully oriented $SrTiO_3$ (106) in Fig. 2. We observe that the density of flux filaments and thus of the ED's increase in YBCO films on substrate surfaces which deviate from the ideal $SrTiO_3$ (106) surface due to an increasing number of macrosteps and irregularities on the substrate surface. Together with a more pronounced filamentary flux pattern and decreasing Δx we observe a decrease of $j_{c,T}$ by a factor of 2 (see Table I).

The microstructure consisting of two kinds of planar defects with different longitudinal pinning force and the related filamentary flux penetration in the L direction is sketched in Fig. 4. In the following the strengthening of the filaments and the decrease of $j_{c,T}$ with increasing structural width of the planar defects is discussed by applying a model of Gurevich and Cooley.[46] At planar defects where the microscopic eddy current of vortices is reduced from the (bulk) depairing current j_0 to the Josephson current $j_{J,0}$, the Abrikosov vortices turn into anisotropic Abrikosov vortices with a highly anisotropic Josephson core. The vortex core of such Abikosov-Josephson (AJ) vortices is elongated along the planar defect with a core radius of

$$\xi_L=\frac{3\sqrt{3}}{4}\frac{j_0}{J_{J,0}}\xi_{ab}, \tag{1}$$

whereas the transverse core radius remains at a size $\xi_T \approx \sqrt{2}\xi_{ab}$.

The longitudinal pinning force per unit length $f_{p,L}$ acting on AJ vortices would vanish for a perfectly homogenous planar defect. A nonvanishing $f_{p,L}$ results from inhomogeneities of $j_{J,0}$, e.g., due to variations in the structural width r_p of the APB's or in their extensions along c axis. A model[46] based on the variation of the Josephson coupling energy of AJ vortices as a function of position within a planar defect gives

$$f_{p,L}=\delta_J\epsilon_0\frac{L}{L^2+\xi_L^2}, \tag{2}$$

with inhomogeneity size L and disorder parameter $\delta_J=\delta j_{J,0}/j_{J,0}$. The line energy of the vortex line is given by $\epsilon_0=\Phi_0^2/(4\pi\mu_0\lambda_{ab}^2)$. The longitudinal pinning force has a maximum when L becomes of the order of the longitudinal core size ξ_L. Assuming a distribution of inhomogeneity lengths L and that the AJ vortices always take that pinning site with maximum $f_{p,L}$, one may set $L\approx\xi_L$ and Eq. (2) gives

$$f_{p,L}\approx\delta_J\epsilon_0\frac{1}{2\xi_L}. \tag{3}$$

This means that the longitudinal pinning force decreases with increasing anisotropy of the AJ vortices. Since the Josephson current of a planar defect with large r_p (ED's) is smaller than that of an APB, according to Eq. (1) the AJ vortices at ED's display larger anisotropies and the $f_{p,L}$ of ED's is smaller than the $f_{p,L}$ of APB's. Within the framework of this simple model, using $j_{c,T}$ values from Table I and assuming $\delta_J\approx0.5$ one obtains for the longitudinal core radius of the AJ vortices $\xi_L\approx5-7$ nm at APB's and $\xi_L\approx15-25$ nm at ED's.

VI. FIELD DEPENDENCE OF j_c

The presence of planar APB's and ED's with different structural width and different longitudinal pinning is also reflected by the magnetic-field dependence of the transverse critical current $j_{c,T}$. According to a model proposed by Gurevich and Cooley,[46] the weakly pinned AJ vortices in the ED's are stabilized by the stronger pinned vortices in their neighborhood, which gives

$$j_{c,T}=j_{c,ED}+c\sqrt{B_z}. \tag{4}$$

At low local magnetic-flux densities, the transverse critical current is given by the lower longitudinal pinning force $f_{p,L}$ (ED) of the ED's,

$$j_{c,ED}\approx f_{p,L}(\mathrm{ED})/\Phi_0. \tag{5}$$

With increasing B_z the weaker pinned anisotropic AJ vortices at the ED's are stabilized by the AJ vortices at the APB's with higher longitudinal pinning force by magnetic interaction. Thus $j_{c,T}$ should increase with increasing local flux density approximately up to a value which is given by the stronger pinning of the APB's.

The field dependence of j_c was investigated by magneto-optical measurements which enable us to a separate $j_{c,L}(B_z)$

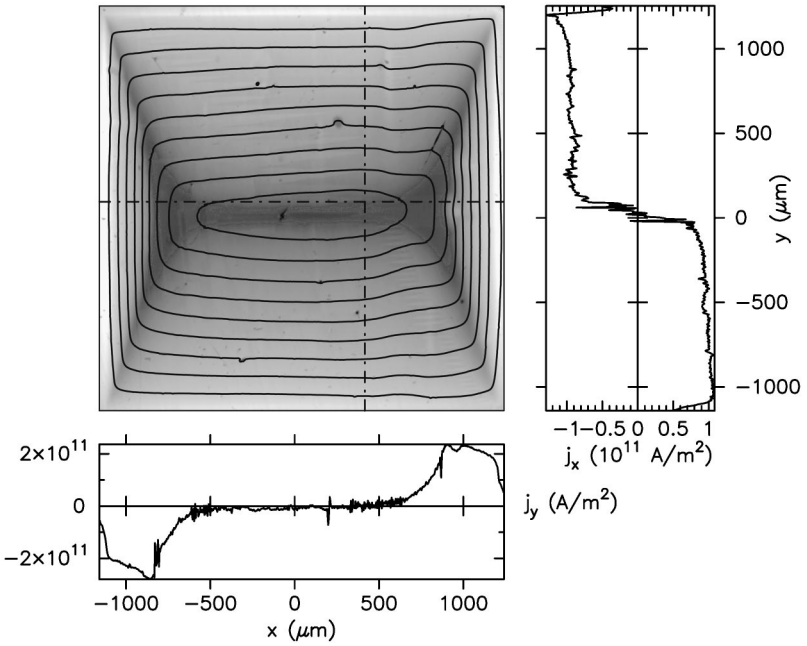

FIG. 5. Flux density distribution in a square-shaped, 320-nm-thick YBCO film (S5) on a not perfectly developed $SrTiO_3$ (106) at $B_{ex}=48$ mT and $T=5$ K. Full lines are indicating the current path and, in addition, the current density profiles are plotted along the dashed lines. Three dark spots are distortions in the MOL.

and $j_{c,T}(B_z)$ up to external fields of $B_{ex}=200$ mT. The average $\overline{j_c}(B_{ex})$ was measured up to fields of 5 T by means of a SQUID magnetometer where a separation of the anisotropic currents is not possible. The investigations were performed on a square-shaped 320-nm-thick YBCO film (sample S5) deposited on a not perfectly developed $SrTiO_3$ (106) surface. The magnetic flux and current distribution for $B_{ex}=48$ mT is visible in Fig. 5. In this film the mean distance between two flux filaments is $\Delta x \approx 30$ μm. Note that they are almost invisible in Fig. 5 due to a lower resolution of the image compared to Fig. 3.

Figure 6(a) shows the dependence of $j_{c,T}$ and $j_{c,L}$ on the local magnetic-flux density B_z in the YBCO sample represented in Fig. 5. The curves have been obtained at different external fields by the following method: The flux density distribution $B_z(x,y)$ was measured for each applied external field B_{ex} and the corresponding current-density distributions $j_{c,T}(x,y)$ and $j_{c,L}(x,y)$ have been determined by inversion of Biot-Savart's law. Afterwards for each fixed B_{ex} the range of the local $B_z(x,y)$ from its minimum to its maximum was divided in 100 channels and for the entire film the average $j_{c,T}$, respectively, $j_{c,L}$ was determined in each B_z channel.

Within the experimental accuracy all curves determined for different B_{ex} in Fig. 6(a) yield a unique local-field dependence for $j_{c,T}$ and $j_{c,L}$, respectively. The transverse critical current is enhanced with increasing local field B_z up to $B_{z,max} \approx 95$ mT. The $j_{c,T}$ enhancement with increasing flux density from the flux front towards the film edges is also visible in the current-density profile of $j_x(y)$ in Fig. 5. In Fig. 6(a) $j_{c,T}(B_z)$ displays an increase in the field range $0 \leqslant B_z \leqslant 10$ mT followed by a smooth further enhancement at larger B_z. This behavior is not described by Eq. (4) which is valid for mediate fields $B_{c1} \ll B_z \ll B_{c2}$.[46] Therefore only the smoothly increasing part of $j_{c,T}(B_z)$ was fitted by Eq. (4) giving $j_{c,ED}=5.6\times10^{10}$ A/m^2 and $c=1.6\times10^{11}$ A/(m^2 T$^{1/2}$). In fact, for $B_z \to 0$ the measured $j_{c,ED} \approx 3\times10^{10}$ A/m^2 is significantly smaller than the result of the fit. In contrast to $j_{c,T}(B_z)$, $j_{c,L}(B_z)$ decreases with increasing local field. The increasing part of $j_{c,L}(B)$ at small B_z represents the cross over from the screening currents $j_s < j_c$ in the flux free area of the sample to the critical currents.

Since the application of this quantitative analysis of the local-field dependence of j_c is restricted to $B_z < 120$ mT due to the onset of saturation of the iron garnet MOL, we investigated the difference in the field dependence of both current components by the change of the mean anisotropy ratio A_j

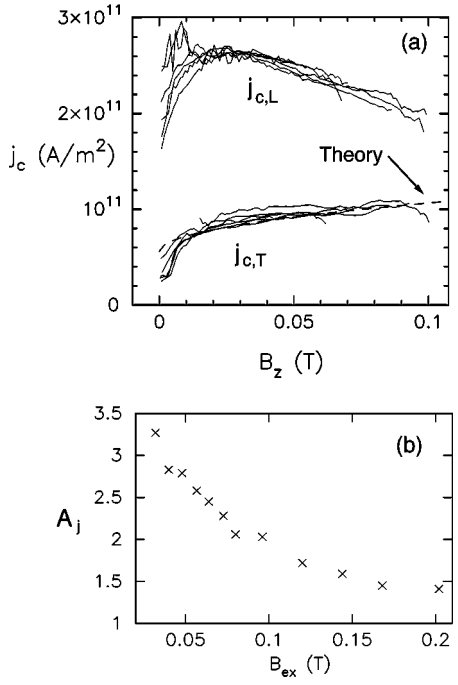

FIG. 6. (a) Dependence of $j_{c,T}$ and $j_{c,L}$ on the local magnet flux density B_z at different external fields $B_{ex}=32$, 40, 48, 56.8, 64, and 80 mT and $T=5$ K determined as described in the text. The theoretical curve is calculated from Eq. (4) with $j_{T,ED}=5.6\times10^{10}$ A/m^2 and $c=1.6\times10^{11}$ A/(m^2 T$^{1/2}$). (b) Change of the anisotropy ratio A_j of the critical currents as a function of the applied external field B_{ex} at 5 K.

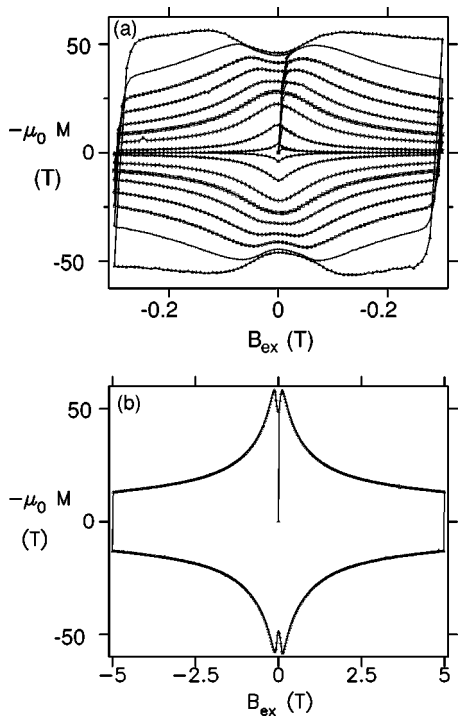

FIG. 7. (a) Low-field magnetization curves of the sample (S5) presented in Fig. 5 for different temperatures $T=5$, 15, 25, 35, 46, 55, 64, 76, and 85 K. For each temperature the samples was cooled down from $T>T_c$ in zero field and a full hysteresis was measured. (b) High-field magnetization curve of the same sample at $T=5$ K.

$=\overline{j_{c,L}}/\overline{j_{c,T}}$. According to Forkl and Kronmüller[36] in square-shaped films A_j can be determined by observing the angle α between a discontinuity line and a square edge (parallel to $j_{c,L}$). Simple geometrical considerations lead to $A_j=1/\tan\alpha$. This method enables an observation of the anisotropy ratio even for magnetic fields where the MOL is already saturated. It has the disadvantage that one is restricted to determine an average value of A_j for each B_{ex}. Figure 6(b) shows the anisotropy ratio A_j at different applied external fields up to 200 mT at 5 K. The increase of $j_{c,T}$ with local field together with the decrease of $j_{c,L}$ results in a drastic decrease of the mean anisotropy ratio A_j with increasing external field.

The increase of $j_{c,T}$ with increasing field is also reflected by the magnetization curves presented in Fig. 7. Figure 7(a) shows the magnetization M normal to the film plane for different temperatures in a magnetic field range of $B_{ex}=\pm 300$ mT. In Fig. 7(b) the $M(B_{ex})$ hysteresis is presented for applied fields up to ± 5 T at 5 K. The low-field magnetization curves in the temperature range between $T=5$ and 35 K displays a significant minimum of the remanent magnetization for $B_{ex}\rightarrow 0$ which is not observed at YBCO film on well oriented substrates.[47] This effect vanishes at higher temperatures. Magneto-optical measurements reveal that in the higher temperature regime $T>35$ K the flux filaments are not visible and thus the minimum in $M(B_{ex})$ for $T<35$ K is clearly correlated to the presence flux filaments. However, in this article we focus on the low-temperature behavior.

The low-field increase of $M(B_{ex})$ is due to two different effects both related to the increase of $j_{c,T}$ with local field: (i) With increasing B_{ex} the B_z distribution in the film is shifted to larger fields yielding a larger average $j_{c,T}$. (ii) Due to the decreasing $A_j(B_{ex})$ the discontinuity lines are moved towards the sample center and the area where the larger $j_{c,L}$ is flowing is increased. However, since $\mathbf{M}\propto\mathbf{r}\times\mathbf{j}$ the currents at the sample edges mainly contribute to M and (i) should dominate over (ii). Within this assumption, one derives from magnetization measurement, that $j_{c,T}$ at the sample edges reaches its maximum at $B_{ex}\approx 125$ mT at 5 K. Using the fit of Eq. (4) and assuming $B_{z,max}\approx 125$ mT we yield a maximum $j_{c,T}\approx 1.2\times 10^{11}$ A/m^2. This represents the maximum $j_{c,T}$ crossing the ED's where the pinning of the AJ vortices is stabilized by magnetic interaction of stronger pinned AJ vortices at APB's.

Finally, we want to discuss the high-field behavior of M in Fig. 7(b) together with the average critical current density $\overline{j_c}$ in the film. Since the magnetization measurement measures mainly the currents at the film edges, the different sizes of the areas where $j_{c,L}$ or $j_{c,T}$ is flowing can be neglected and one has

$$\overline{j_c}\approx\frac{j_{c,L}+j_{c,T}}{2}\approx\frac{3M}{w}, \tag{6}$$

where w denotes the half sample width. For the maximum $M=60$ T at 5 K and $B_{ex}=125$ mT one obtains $\overline{j_c}\approx 1.6\times 10^{11}$ A/m^2. This result agrees with the average $\overline{j_c}=1.55\times 10^{11}$ A/m^2 using the $j_{c,L}$ and $j_{c,T}$ values from Fig. 6(a) at $B_z=90$ mT. From $M(B_{ex})$ in Fig. 7(b) follows, that the average critical current is reduced to $\overline{j_c}\approx 0.3\times 10^{11}$ A/m^2 at $B_{ex}=5$ T. However, it cannot be detected by this measurement whether $j_{c,L}$ or $j_{c,T}$ is more sensitive on large magnetic fields.

The strong-field dependence of $j_{c,L}$ in Fig. 6(a) already occurring for small fields seems to be surprising if one considers the matching field $B^*\approx 60$ T of an array of APB's with a mean distance of 6 nm. However, the determination of the matching field of an array of planar defects is a very complex problem since the anisotropy of the defects and the AJ vortices has to be considered. For magnetic fields, where the vortex cores of the AJ vortices start to overlap in L direction, $j_{c,T}$ crossing the boundaries should be drastically reduced. From the estimated core radius of the AJ vortices longitudinal to the defect planes one yields an overlapping of the vortex cores at APB's at fields between 24 and 12 T ($\xi_L=5$–7 nm) and at ED's at fields between 2.6 T and 950 mT ($\xi_L=15$–25 nm). However, both estimates cannot explain the decrease of $j_{c,L}$ at very small fields. In contrast to the low-field behavior of $j_{c,T}$ which is nicely understood, more investigations as well as theoretical work are necessary to understand the high-field behavior of j_c at arrays of planar defects.

VII. ANGULAR DEPENDENCE OF j_c

In the following section we determine the critical current as a function of its angle α_j to the APB's. The successive transition of the current density within the superconducting film plane $\mathbf{j}(\alpha_j)=[j_T(\alpha_j),j_L(\alpha_j),0]$ from $j_{c,T}=j_T(\alpha_j$

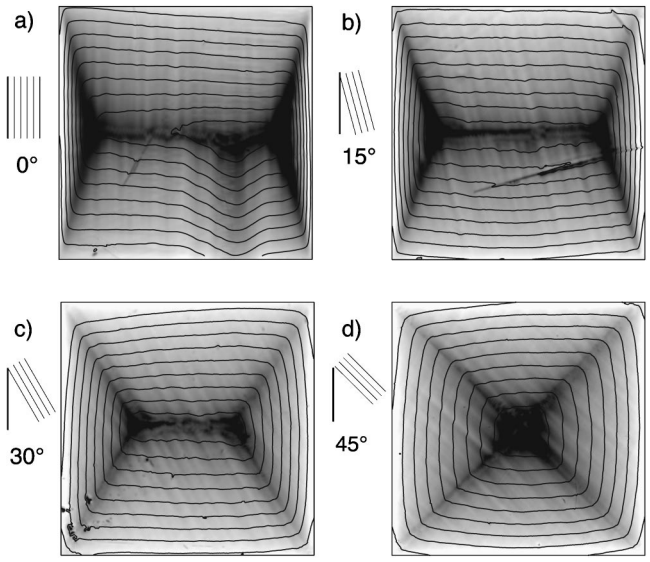

FIG. 8. Magneto-optically observed flux density distribution and superimposed current stream lines of four squares patterned in different orientations from one YBCO film on $SrTiO_3$ (106). The measurements were done at $B_{ex}=24$ mT and $T=5$ K. The angles α_j between the T direction of the APB's and one edge of the square are depicted at each image. In (a) and (b) the MOL has a defect which is visible as a dark line.

$=0°$) to $j_{c,L}=j_L(\alpha_j=90°)$ is investigated. By varying the angle of $\mathbf{j}$ with respect to the APB's plane we probe the angular dependence of the pinning force of these planar defects. For tailoring the flow direction of the current we use the condition that the current flows parallel to the sample edges.

For the measurement of $\mathbf{j}(\alpha_j)$, we used two YBCO films on $SrTiO_3$ (106). The first film ($t=280$ nm) was patterned by chemical etching four 900-μm-wide squares having differently oriented film edges with respect to the APB's. The orientation of the square edges to the T direction of the APB's was varied by angles of $\alpha_j=0$, 15, 30, and 45°. Because of div$\mathbf{j}=0$ the current flows parallel to the film edges with an angle α_j to the APB's. The second film was patterned to a disk with a radius of $R=1$ mm. By this disk geometry, the angle of the current cover the full range 0

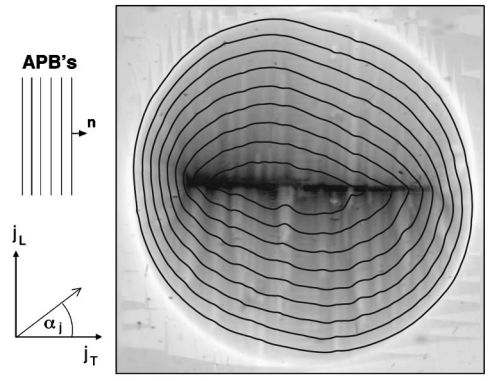

FIG. 9. (a) Magneto-optically observed flux density distribution and superimposed current stream lines in a disk-shaped YBCO film grown on $SrTiO_3$ (106) at $B_{ex}=28$ mT and $T=5$ K.

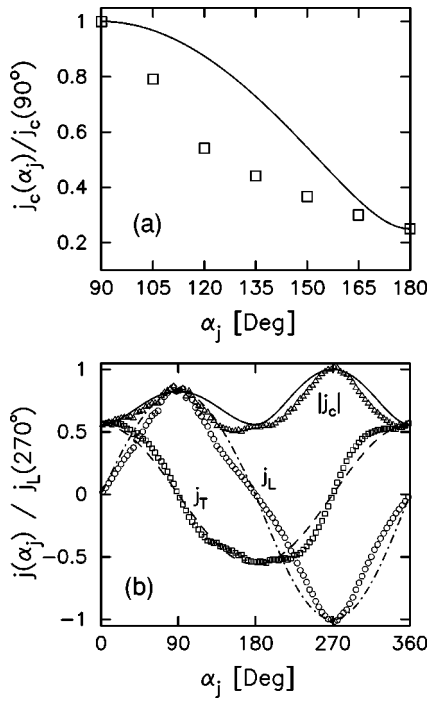

FIG. 10. (a) Angular dependence of j_c for the four differently oriented squares visible in Fig. 8. (b) Angular dependence of $|j_c|$ and of the components j_L and j_T in the L and T directions, respectively, for the disk of Fig. 9. In addition, the elliptical angular dependence following from Eqs. (7) is plotted as bold and broken lines.

$\leqslant\alpha_j\leqslant 360°$ with respect to the normal vector $\hat{\mathbf{n}}$ (T direction) of the APB's.

Figure 8 shows the magnetic-flux density distribution and the superimposed current stream lines for the four YBCO squares with different orientations. The orientation of the planar defects is visible by looking at the orientations of the flux filaments. For all four squares the flux filaments are oriented parallel to the boundaries. The mean anisotropy ratio of the current densities changes from $A_j=4(0°)$, over $A_j=2.6(15°)$, $A_j=1.75(30°)$ to $A_j=1(45°)$. Qualitatively this can be recognized also from the shift of the the discontinuity lines from a ''double Y'' to an ''X''-like pattern. For the disk-shaped YBCO film, the magnetic-flux density distribution and the superimposed current stream lines are visible in Fig. 9.

The angular dependence of j_c from the squares is depicted in Fig. 10(a). For the disk $|j_c|(\alpha_j)$ together with the current-density components j_L and j_T flowing in the L and T direction, respectively, is plotted in Fig. 10(b). The angle α_j of the current was determined by calculating j_L and j_T by inversion of Biot-Savart's law from the flux distribution and using $\alpha_j=\tan^{-1}(j_L/j_T)$. The values which are measured at the squares and the disk are very similar and the angular dependence normalized to the value at $\alpha_j=90°$ is nearly the same.

Remarkably, the observed angular dependence of j_c is not given by the vector superposition of the $j_{c,T}(\alpha_j=0°)$ and $j_{c,L}(\alpha_j=90°)$ components. This would result in the elliptical angular dependence

$$j_L(\alpha_j)=j_{c,L}\cos(\alpha_j),$$

$$j_T(\alpha_j)=j_{c,T}\sin(\alpha_j),$$

$$j_c(\alpha_j)=[j_{c,L}^2\cos^2(\alpha_j)+j_{c,T}^2\sin^2(\alpha_j)]^{1/2}, \quad (7)$$

which is plotted as bold (j_c), dashed (j_T) and dashed-dotted lines (j_L) in Fig. 10.

We will show in the following section that the deviation of the angular dependence from an elliptical one can be understood in terms of quasiparticle scattering in superconductors with anisotropic gap. The additional scattering which occurs for a current component crossing the defect planes ($\alpha_j \neq 90°$) results in a depletion of the superconducting charge density n_s between the planes. This affects not only the current component j_T crossing the planes. The depletion of n_s modifies also the current component j_L flowing parallel to the APB's, which gives a stronger decrease than $j_L \propto \cos(\alpha_j)$.

VIII. THEORY OF TRANSVERSE PINNING MECHANISMS

In order to analyze the observed angular dependence of j_c together with the extraordinary large $j_{c,L}$ up 8.5×10^{11} A/m^2 the possible transverse pinning mechanisms of vortices at APB's are discussed in the following. We give for each pinning mechanism an approximate calculation of the transverse component of the pinning force $f_{p,T}$ when probed by an angular dependent driving force corresponding to an angular dependent current density. Pinning at planar defects may occur by magnetic interaction, where the deformation of the eddy currents of a vortex as a function of the distance to the defect plane gives rise to a pinning potential.[46] Core pinning may take place by a direct suppression of superconductivity which gives rise to fluctuations in T_c (δT_c pinning). Another indirect mechanism also leads to a pinning potential, where the superconducting state is affected by the scattering of quasiparticles. Whereas in isotropic *s*-wave superconductors nonmagnetic scattering affects only the kinetic energy of vortex eddy currents, in HTS's elastic scattering results in a change of condensation energy due to the presence of an anisotropic gap.

A. Magnetic pinning

For the approximate calculation of the pinning force of vortices in an array of parallel oriented planar defects with mean distance of ≈ 6 nm, we consider a single vortex nearby a planar defect which energy is modified due to a deformation of the eddy current distribution at the boundary. According Gurevich and Cooley[46] the transverse pinning force of a vortex at a distance $\xi_{ab}<x\ll\xi_L$ is given by

$$f_{p,T}(x)=-\frac{1}{x}\epsilon_0, \quad (8)$$

where $\epsilon_0=\Phi_0^2/(4\pi\mu_0\lambda_{ab}^2)$ is the self-energy of the vortex line per unit length and λ_{ab} denotes the magnetic penetration depth in the (ab) plane for a defect free superconductor.

For a vortex placed at a distance of some nm from a single APB interacting with the boundary by magnetic interaction one easily calculates from Eq. (8) longitudinal critical current densities $j_{c,L}\approx 1-2\times10^{12}$ A/m^2. However, comparing the magnetic size of a vortex with the mean distance between APB's of 6 nm, the interaction of a vortex with several boundaries must be taken into account. Since theoretical simulations of this effect are not available at present and the maximum of the eddy current of a vortex parallel to the boundary is located at $\approx\sqrt{2}\xi_{ab}$ from the core center we regard Eq. (8) as rough approximation giving the correct order of magnitude of the pinning force. Consequently, magnetic pinning may principally account for the observed large $j_{c,L}$.

When exerting an angular dependent driving force on a vortex at a distance x_0 to the boundary, the angular dependence of the pinning force according to Eq. (8) is given by the angular variation of its distance to the APB's plane $s=x_0/\cos(\alpha_j)$. This leads to $j_L\propto\cos(\alpha_j)$ and thus results in the same elliptical angular dependence as already given by Eq. (7) and is in contradiction to the observed angular dependence in Fig. 10.

B. Core pinning by δT_c effect

As already discussed in a former section, an Abrikosov vortex at a planar defect with a locally reduced transverse supercurrent $j_{J,0}<j_0$ is strongly deformed and turns into a so-called Abrikosov-Josephson (AJ) vortex with highly anisotropic vortex core with a core radius ξ_L longitudinal to the boundary given by Eq. (1). We assume that the structure of the AJ vortex at the planar defect is completely determined by the deformation of the vortex eddy currents and calculate the order parameter around the vortex core from the current distribution of an AJ vortex in the framework of Ginzburg-Landau (GL) theory. Considering here only the δT_c effect, all additional effects of the boundary, e.g., a decrease of the Ginzburg-Landau coherence length ξ_{ab} due to quasiparticle scattering are neglected.

The magnetic structure of the AJ vortex is obtained by slightly modifying a model of Gurevich and Cooley.[46] In extension to their model, our modification takes into account that the radius of the vortex core ξ_T perpendicular to the defect plane is finite. The field distribution of an AJ vortex at an infinitely thin planar defect at $x=0$ is given in the framework of London theory by

$$B_z-\lambda^2\left[\frac{\partial^2 B_z}{\partial x^2}+\frac{\partial^2 B_z}{\partial y^2}\right]=\Phi_0\delta(x)\delta(y)+\frac{\Phi_0}{2\pi}\frac{\partial\varphi}{\partial y}\delta(y). \quad (9)$$

The second term on the right side of Eq. (9) takes the boundary condition of a Josephson junction into account. In order to calculate the structure of the vortex core in the framework of Ginzburg-Landau theory we replace $\delta(x)\delta(y)$ by a function $W(x,y)$ resulting in a finite core size. It is chosen by the condition that in the limit $j_{J,0}\rightarrow j_0$ an isotropic Abrikosov vortex is recovered by the theory. However, it is not necessary to calculate explicitly $W(x,y)$, since a special solution of Eq. (9) without the boundary term is given analytically by Clem.[48] We use the Green's-function method to calculate the general solution of Eq. (9).

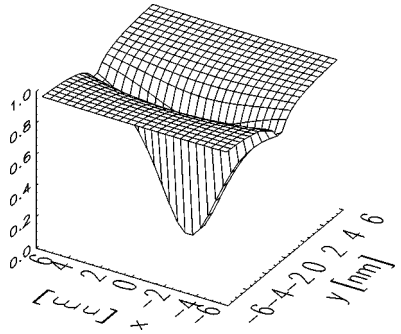

FIG. 11. Normalized order parameter at the vortex core of an AJ vortex at an infinitely thin planar defect with T_c suppression. The anisotropy of the vortex core is $\xi_L/\xi_{ab}=15$.

The phase kink of the AJ vortex at the planar defect at $x=0$ is given by $\varphi(y)=2\tan^{-1}(y/\xi_L)+\pi$,[46] and one obtains approximately for small x,y

$$B_z(x,y)=\gamma\ln\left[\frac{4\lambda_{ab}^2}{[y^2+(|x|+\xi_L')^2+\xi_T^2]^{1/2}}\right]-2\gamma C. \quad (10)$$

$C\approx 0.577$ represents the Euler constant and $\gamma=\Phi_0/2\pi\lambda_{ab}^2$. To obtain the correct isotropic limit, the longitudinal core radius must be renormalized to $\xi_L'=\xi_L-\xi_T$. The structure function $f(x,y)$ of the vortex core, defined by $\Psi(x,y)=f(x,y)\Psi_\infty$, is then calculated by GL theory:

$$f^2(x,y)=\frac{-j_x(x,y)}{\Psi_\infty^2\left[\frac{2\hbar e}{m}\frac{\partial\varphi(x,y)}{\partial x}+\frac{4e^2}{m}A_x(x,y)\right]}. \quad (11)$$

The current-density components j_x and j_y are obtained from Eq. (10) by Ampère's law, giving

$$j_x(x,y)=\frac{\gamma}{\mu_0}\frac{-2y}{y^2+(|x|+\xi_L')^2+\xi_T^2}, \quad (12)$$

$$j_y(x,y)=\frac{\gamma}{\mu_0}\frac{2(|x|+\xi_L')\mathrm{sgn}(x)}{y^2+(|x|+\xi_L')^2+\xi_T^2}.$$

The vector potential $\mathbf{A}$ is obtained by numerically integrating the field distribution Eq. (10) and using the Coulomb gauge. The derivative of the phase distribution $\varphi(x,y)$ is approximately given by

$$\frac{\partial\varphi}{\partial x}\approx\frac{2e}{\hbar}\frac{[j_yA_x-j_xA_y]\left(\frac{\partial j_x}{\partial x}y-\frac{\partial j_y}{\partial x}x-j_y\right)}{j_x^2+j_y^2}. \quad (13)$$

Figure 11 shows the calculated order parameter $f(x,y)=\Psi(x,y)/\Psi_\infty$ for an anisotropy ratio of the vortex core of $\xi_L/\xi_{ab}=15$.

The angular pinning force density is calculated using polar coordinates (r,α_j) from the maximum of the spatial derivative of the pinning potential by

$$f_p(\alpha_j)=|\partial U_p(\alpha_j,r)/\partial r|_{max}, \quad (14)$$

with

$$U_{p,T_c}=\epsilon_0\frac{L_p}{t}f^2(r,\alpha_j)\frac{\delta T_c}{T_c}. \quad (15)$$

The pinning potential U_{p,T_c} is generated by the variation of the transition temperature $\delta T_c/T_c$ at the planar defect. Since a single APB is not extended through the entire film with thickness t along the c axis, L_p/t denotes the pinned part of a vortex.

C. Quasiparticle scattering pinning

In the framework of microscopic quasiclassical pinning theory, developed by Thuneberg[22] and generalized by Friesen,[30] the pinning energy per unit length of an infinitely thin planar defect with transport scattering cross section of quasiparticles $\sigma_{tr,T}$ transverse to the boundary is given by

$$U_p(r)=\xi_0\sigma_{tr,T}\frac{N(0)}{2t}|\Delta_d|^2f^2(r)F[\rho_i,\langle\phi(\mathbf{k})\rangle], \quad (16)$$

where the active scattering cross section per vortex at the boundary is estimated to $\sigma_{tr,T}=p_{tr,T}2\xi_{ab}L_p$. We consider only the transverse component of the transport scattering probability tensor and neglect diffuse scattering, so $p_{tr,T}=1-\tau$ is determined by the transmission probability of the plane τ. L_p denotes the pinned length of a vortex, ξ_0 the BCS-coherence length, and t the thickness of the superconducting film. The dimensionless function $F\propto 1-\langle\phi(\mathbf{k})\rangle$ depends as well on the Gorkov disorder parameter $\rho_i=\xi_0/l$ as on the normalized symmetry function of the gap $\phi(\mathbf{k})$. For a pure d-wave order parameter, the Fermi-surface average over $\phi(\mathbf{k})\propto k_x^2-k_y^2$ gives $\langle\phi\rangle=0$ and thus $F=1$ is maximized.

In contrast, for an isotropic s-wave superconductor the symmetry function is $\phi(\mathbf{k})=1$ and the Fermi-surface average gives $\langle\phi\rangle=1$. This leads to $F=0$ and only a second-order term contributes to the pinning energy[22]

$$U_p(r)=\frac{2}{3}\xi_0\sigma_{tr,T}\frac{N(0)}{t}\frac{\partial\chi(\rho_i)}{\partial\rho_i}\xi_0^3\left|\frac{\partial\Delta(r)}{\partial r}\right|^2. \quad (17)$$

Here $\chi(\rho_i)\approx 0.95\Sigma_{n=0}^{\infty}[(2n+1)^2(2n+1+\rho_i)]^{-1}$ represents the Gorkov function. Whereas in superconductors with anisotropic gap, the order parameter is suppressed by quasiparticle scattering at small defects[30] with size $r_p\geqslant k_f^{-1}\approx 0.1\xi_{ab}$, nonmagnetic scattering in isotropic superconductor increases order-parameter gradients nearby a boundary and thus the kinetic energy of the eddy currents of a vortex. This is equivalent to a decrease of the Ginzburg-Landau coherence length $\xi_{ab}(0)=\xi_0\sqrt{\chi(\rho_i)}/1.36$ or to H_{c3} effects at superconductor surfaces or interfaces.

For the calculation of the angular dependence of j_c we use GL theory where the coarse graining over the length scale ξ_{ab} gives

$$U_{p,\delta l}=\int d^2r'\,\delta\alpha(r')\frac{L_p}{t}\Psi_\infty^2f(r-r')^2, \quad (18)$$

for anisotropic and

$$U_{p,\delta l}=\frac{\hbar^2\Psi_{\infty 2}}{2m^*}\int d^2r'\,\delta\chi[\rho(r')]\frac{L_p}{t}\left(\frac{\partial f(r-r')}{\partial r'}\right)^2 \quad (19)$$

for isotropic gap.

In the case of anisotropic gap, the pinning potential Eq. (18) is due to quasiparticle scattering induced spatial variation of the first Ginzburg-Landau coefficient $\delta\alpha(r') = 4e^2\mu_0^2 H_c^2 \lambda_{ab}^2 \delta\chi(r')/m^*$ which we approximate by the variation of the Gorkov function $\delta\chi\{\rho_i[l(r)]\}$ due to the variation of the mean free path $l(r)$. In addition, the condensate outside the vortex core and the boundary $\Psi_\infty^2 = m^*/(4\mu_0\lambda^2 e) = n_s[l(r)]$ is depleted by the additional QP scattering if a current component is crossing the boundary. This leads to an overall reduction of the maximum current density j_0. Theory suggests[28]

$$n_s \propto \lambda^{-2} \propto (1 + 0.79\Gamma^{+1/2})^{-2}, \tag{20}$$

considering a *d*-wave superconductor. The dimensionless scattering parameter is given by $\Gamma(\alpha_j) = \hbar v_F / [2l(\alpha_j) k_B T_c)]$; k_B denoting the Boltzmann constant.

In the case of isotropic gap, the first-order term Eq. (18) vanishes and the second-order term Eq. (19) gives a pinning potential by the spatial variation of $\delta\chi(r)$ leading to a variation of the kinetic energy. In this case, ψ_∞ is not affected by nonmagnetic scattering which is equivalent to the so-called Anderson theorem.[25]

The angular dependence of the single vortex pinning force is given by Eq. (14). For the order parameter at the vortex core an ansatz $f^2(r) = 1 - \exp(-r^2/2\xi_T^2)$ developed by Welch[49] was used, avoiding singularities in the integrals. Setting $\xi_T = 1.85\xi_{ab}$ one yields the same maximum gradient of $f(r)$ at the vortex core as in the model of Clem.[48] The angular mean free path $l(\alpha_j)$ at a distance x_0 from a single planar defect with transport scattering probability $p_{tr,T}$ is given by[50]

$$l(r, \alpha_j) = l_0(1 - p_{tr,T} e^{[-s(\alpha_j)/l_0]}), \quad -90 \leqslant \alpha_j \leqslant +90\,^\circ, \tag{21}$$

where l_0 denoting the mean free path without planar defects due to background disorder and $s(\alpha_j) = x_0/\cos(\alpha_j)$ the variation of the distance to the boundary with angle α_j. To extend this model to an array of planar defects, we consider a charge carrier at a position x traveling between two planar defects located at x_1 and x_2, both with the same transverse transport scattering probability $p_{tr,T}$. The summation law of mean free paths is $l^{-1} = l_1^{-1} + l_2^{-1}$, where l_1 and l_2 are obtained from Eq. (21) respectively, giving

$$l(x, \alpha_j) = 2l_0 \frac{(1 - p_{tr,T} e^{-s_1/2l_0})(1 - p_{tr,T} e^{-s_2/2l_0})}{2 - p_{tr,T} e^{s_1/2l_0} - p_{tr,T} e^{s_2/2l_0}}, \tag{22}$$

with $s_1 = |x - x_1|/\cos\alpha_j$ and $s_2 = |x - x_2|/\cos\alpha_j$.

D. Comparison to experiment

Since our calculation of the angular dependence of the pinning force considers only the transverse $f_{p,T}$ probed by an angular dependent driving force, Fig. 12 shows the experimentally observed $j_L(\alpha_j)$ in the range $90 \leqslant \alpha_j \leqslant 180\,^\circ$ from Fig. 10 together with the theoretical curves following from different pinning mechanism. For δT_c pinning, the calculated $j_L(\alpha_j)$ curves for different anisotropies of the vortex core $\xi_L/\xi_T = 1.8,\ 4.7$, and 30 are depicted.

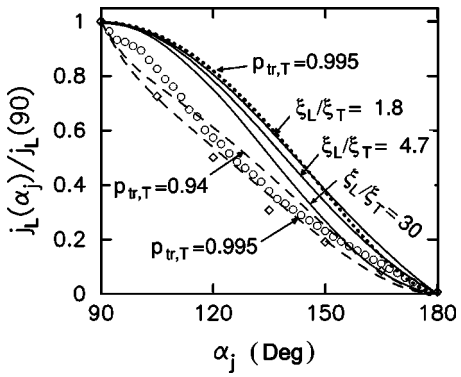

FIG. 12. Comparison of measured and calculated angular dependence of j_L for $90 \leqslant \alpha_j \leqslant 180\,^\circ$. The measured data is represented as ○ for the disk and as ◇ for the squares. For δT_c pinning, $j_L(\alpha_j)$ is plotted with different anisotropies ξ_L/ξ_T of the AJ-vortex core as indicated in the plot (full lines). The dotted line corresponds to the δl pinning without pair breaking (isotropic *s* wave) and the dashed lines to δl pinning via condensation energy, when pair breaking is present.

For the quasiparticle scattering pinning via kinetic energy, when the condensate is not depleted by scattering, the $j_L(\alpha_j)$ is very similar to the curves obtained from δT_c pinning. All of them exhibit an initial slope of $(\partial/\partial\alpha_j) j_L|_{\alpha_j = 90\,^\circ} = 0$ which obviously deviates from the measured data. The calculated angular dependence following from these two pinning mechanism only slightly deviates from $j_L \propto \cos(\alpha_j)$ which was proposed at first thought in Eq. (7) and which follows also approximatively from magnetic pinning.

In contrast, the calculated angular dependence of $j_L(\alpha_j)$ for δl pinning via condensation energy describes well the measured data nearly in the full angular range. The strong decrease of j_L for increasing $\alpha_j > 90\,^\circ$ reflects the additional scattering of quasiparticles when an increasing current component starts to cross the boundaries. This affects the whole condensate between the 6 nm spaced defects and thus reduces the longitudinal current density j_L for $\alpha_j > 90\,^\circ$.

IX. ORDER-PARAMETER SUPPRESSION AT APB'S

In Ref. 12 we already presented the temperature dependence of both current components $j_{c,T}$ and $j_{c,L}$. In addition to the angular dependence of j_L the observed Ambegaokar-Baratoff-like temperature dependence[51] of $j_{c,T}$ is an unambiguous indication for the presence of tunneling phenomena for the current crossing the boundaries and thus for an order-parameter suppression at APB's. We want to come back now to the observed magnitudes of $j_{c,L}$ and $j_{c,T}$ and discuss the order-parameter suppression at APB's. This gives additional evidence for the QP scattering pinning mechanism.

Let us first discuss a possible pure δT_c effect at the APB's. In general, there are some difficulties in explaining, how planar defects can exhibit large transverse pinning forces together with relatively large $j_{c,T}$. The longitudinal critical current density is given for correlated pinning and small magnetic fields by Eq. (14) in the limit $\alpha_j \to 90\,^\circ$, yielding

$$j_{c,L} = \frac{1}{\Phi_0} f_{p,T}(\alpha_j = 90\,^\circ) \approx \frac{\epsilon_0}{\xi_{ab}\Phi_0} \frac{L_p}{t} \frac{\delta T_c}{T_c}. \tag{23}$$

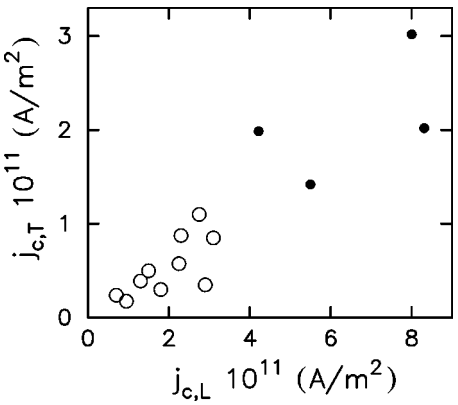

FIG. 13. Correlation between the measured $j_{c,T}$ and $j_{c,L}$ for YBCO films having APB's with a small $r_p=0.7$ nm (full circles) and with APB's exhibiting a larger structural width (ED's) (open circles). The data is also represented in Table I.

We already estimated[11] that $j_{c,L}\approx 8\times 10^{11}$ A/m^2 would require at least $\delta T_c/T_c\approx 0.22$ ($\delta T_c\approx 20$ K) when we assume that the vortices are pinned over their full length $L_p/t=1$. Realistic estimates of their pinned part (due to the finite length of the APB's parallel to the c axis) must assume a much higher T_c suppression of $\delta T_c/T_c\approx 0.3$–$0.4$ in order to explain the large observed $j_{c,L}$. Modeling the defect plane as a normal-superconducting interface, the variation of the order parameter $d\psi/dx\approx\psi_\infty/b$ is given by the linear extrapolation length b.[52] Using the expression $b\approx\xi_{ab}^2/a$ (Ref. 1) with a lattice constant in the (ab) plane of $a=0.39$ nm, one yields $b\approx 5.9$ nm.[11] In the framework of linear extrapolation and using $\delta T_c/T_c\approx 0.3$–$0.4$, one obtains a length scale of order parameter suppression of $d\approx b\,\delta T_c/T_c\approx 1.8$–$2.4$ nm on each side of an APB. Comparing this length with the mean distance of APB's of ≈ 6 nm, a significant part of the superconductivity in the YBCO films should be suppressed and the possibility of large $j_{c,L}$ seems to be questionable. Moreover, the $T_c\approx 89$ K of these samples is only slightly lower than the T_c in YBCO single crystals.

Next, we want to analyze the relation between large $j_{c,T}$ and strong transverse pinning in the framework of the δT_c effect. The Josephson tunneling current through a boundary $j_{J,0}$ depends exponentially on the width of the tunneling barrier d which can be estimated in linear approximation (for small T_c suppressions) to be $d\approx(\delta T_c/T_c)b$ giving

$$j_{J,0}\approx j_0 e^{-d/b}=j_0 e^{-\delta T_c/T_c}. \tag{24}$$

Consequently, an increasing $\delta T_c/T_c$ which is required in the framework of δT_c pinning for large $j_{c,L}$ would necessarily lead to a decreasing $j_{c,T}$. According to Eqs. (3) and (1) together with Eq. (24) one obtains

$$j_{c,T}\propto\xi_L^{-1}\propto j_{J,0}\propto e^{-\delta T_c/T_c}, \tag{25}$$

and $j_{c,T}$ should decrease exponentially with increasing transverse pinning force (increasing $j_{c,L}$). Figure 13 shows the measured $j_{c,T}$, plotted as a function of the measured $j_{c,L}$ for YBCO films with APB's of different structural width r_p. The largest $j_{c,T}$ are observed at the samples where $j_{c,L}$ has extraordinary high values $>4\times 10^{11}$ A/m^2 at $T=5$ K. This observation is in contradiction to the δT_c effect, where by combining Eqs. (23) and (25) one would expect

$$j_{c,T}\propto e^{-j_{c,L}}. \tag{26}$$

In contrast to the δT_c effect, quasiparticle scattering pinning at APB's can account for the large $j_{c,L}$ up 8.5×10^{11} A/m^2 at 5 K as well for the observed $j_{c,T}$ behavior presented in Fig. 13. From the measured anisotropic mean free path of $l_L\approx 70$ nm and $l_T\approx 2$–6 nm in YBCO films on nearly perfect SrTiO 3 (106), where l_T corresponds to the mean distance of APB's, one obtains $p_{tr,T}\approx 1$. Simultaneously, the scattering longitudinal to the boundaries is very low for these films having APB's with $r_p=0.7$ nm. Using Equations (16) and (17) together with Eq. (14) in the limit $\alpha_j\rightarrow 90°$, one has $j_{c,L}\approx 10^{12}$ A/m^2 (kinetic energy) and $j_{c,L}\approx 2.6\times 10^{12}$ A/m^2 (condensation energy) at $T=5$ K. Equations (18) and (19) lead to similar results. Even if only a finite part of the vortices $L_p/t<1$ is pinned at the APB's the observed $j_{c,L}$ is easily calculated by theory assuming QP scattering pinning.

QP scattering at small defects $r_p\ll\xi_0$ induces in d-wave superconductors strong order-parameter suppressions.[26] Consequently, modeling an APB as a planar array of point scatterers, the structural width r_p must not necessarily be in the order of ξ_0 to obtain large transverse pinning forces. In addition, the length scale of the order-parameter suppression d may have smaller values compared to the δT_c effect: A calculation in the framework of microscopic quasiclassical theory shows that the order parameter at a point scatterer may vary by $\delta\Psi/\Psi_\infty\approx 1$ on a length scale of two to three lattice spacings (0.78–1.2 nm).[26] Another argument is given by a microscopic derivation of the GL equations[53,54] which shows that the the GL-coherence length

$$\xi_{ab}(0\text{ K})\approx 0.74\xi_0\sqrt{\chi} \tag{27}$$

is reduced by QP scattering. Thus sharp gradients of the order parameter are sustained by this mechanism.[50] In Eq. (27) χ is denoting the Gorkov impurity function. Using these results, the behavior of $j_{c,L}$ and $j_{c,T}$ in Fig. 13 is qualitatively understood. As long as the current is flowing parallel to the boundaries and r_p is small compared to the defect distance, the order parameter between the 6 nm spaced APB's is less affected by this mechanism compared to the δT_c effect. Due to a strong order-parameter suppression on a small length scale $d\ll\xi_0$ one has a large $j_{c,L}$ as well as large $j_{c,T}$. This is sketched qualitatively in Fig. 14. However, if r_p reaches ≈ 2 nm, the order parameter at the ED's is suppressed on a length scale d, and in addition, the longitudinal scattering $p_{tr,L}$ may not be neglected any more, especially for boundaries with roughness and kinks. This leads to a scattering induced overall reduction of the superconducting charge density as already observed by others.[24]

X. CONCLUSIONS

To summarize our results, planar defects as APB's represent very effective pinning sites for correlated pinning of vortices in HTS's and can account to carry critical currents up to 30% of the depairing current longitudinal to the defect. The combined investigation of magnitude and angular de-

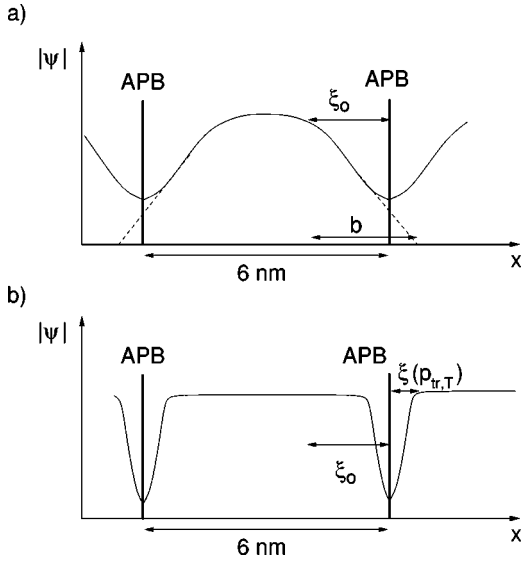

FIG. 14. Schematic drawing of the order-parameter suppression due to (a) δT_c effect and (b) quasiparticle scattering at a planar defect.

pendence of j_c in our model system of parallel oriented planar APB's with small r_p demonstrates the QP scattering as the dominant pinning mechanism being responsible for the extraordinary large magnitude of $j_{c,L}$. Since $p_{tr,T}$ is large and $p_{tr,L}$ is low, this effect causes a suppression of the transverse order parameter on a smaller length scale compared to δT_c pinning and thus strong transverse pinning. In contrast, due to the smooth interface which is confirmed by the large l_L and the Ambegaokar-Baratoff like temperature dependence of $j_{c,T}$,[12] the longitudinal order parameter is little affected by quasiparticle scattering as long as the current is flowing parallel to the boundaries. The strong drop of $j_L(\alpha_j)$ by slightly changing the direction of the current flow confirms that a low scattering rate is crucial for the large $j_{c,L}$ since pair breaking would reduce the superfluid density in L direction and limit $j_{c,L}$ by depairing.

Considering $j_{c,T}$, we made the remarkable observation that $j_{c,T}=2-3\times10^{11}$ A/m^2 reaches values which are typically observed in high quality YBCO films on well oriented single-crystalline substrates. For this large $j_{c,T}$ a small structural width of the APB's of $r_p=0.7$ nm is essential. The drop of $j_{c,T}$ to values $\leqslant10^{11}$ A/m^2 by introducing ED's with $r_p\approx2$ nm into the system lead to conclusions for the transport properties of general grain boundaries. It was shown by Zandbergen, van den Berg, and Kes[55] that the atomic distortions of (100) mirror twin boundaries are restricted to two unit cells corresponding to a r_p of APB's. In contrast, r_p of [100] rotation twin boundaries is larger due to misfit dislocations. A suppression of $j_{c,T}$ to a half of the bulk j_c was reported at TB's in YBCO single crystals.[8] However, a systematic study of the effect of dislocations and r_p variations on j_c at TB's is still lacking.

At small-angle tilt boundaries, the atomic distortions are strongly localized in dislocation cores where the Cu(1) valence is varying on a length scale of 1 nm.[18] At the same time the boundary sections between the dislocation cores are atomically sharp. Comparing SAGB's with APB's, we conclude that the current limiting properties come from the dislocation cores with a larger r_p compared to the boundary itself. A model worked out on this basis, e.g., by Gurevich and Pashitskii,[17] successfully describes the exponential decrease of j_c with grain-boundary angle due to the increasing dislocation content. Our own results in this paper suggests that quasiparticle scattering does not significantly reduce the transverse j_c at smooth and sharp boundaries with $r_p<1$ nm. In contrast, if the distorted regions reach $r_p>1$ nm, a drop of j_c takes place due to a pronounced order-parameter suppression on a larger length scale.

Considering the question whether planar defects contribute to the large pinning in epitaxial YBCO films on well oriented single-crystalline (001) substrates or not, we conclude that a network of planar defects separating the individual growth islands and additional intragranular planar defects as TB's or APB's may be well suited to explain the observed $j_c=1-3\times10^{11}$ A/m^2 at 5 K and at not too large magnetic fields. It is necessary to emphasize that $j_{c,L}$ up to $\approx30\%$ of the depairing current is observed only, if one combines strong transverse pinning together with a low scattering rate $p_{tr,L}(l_L\approx70$ nm) parallel to the current flow. If this is not the case, j_c may be limited due to a QP scattering induced overall depletion of the superconducting condensate.

ACKNOWLEDGMENTS

The authors are grateful to H.-U. Habermeier, J. Zegenhagen, and T. Haage for the preparation of the excellent samples and the intensive cooperation. Thanks also to T. Dragon for the experimental advice and J. Albrecht for stimulating discussions. One of us (Ch.J.) wishes to express thanks to H. C. Freyhardt and M. Friesen for their interest and stimulating discussions.

[1] G. Blatter, M.V. Feigel'man, A.I. Larkin, and V.M. Vinokur, Rev. Mod. Phys. **66**, 1125 (1994).

[2] J. Mannhart, D. Anselmetti, J.G. Bednorz, A. Catana, Ch. Gerber, K.A. Müller, and D.G. Schlom, Z. Phys. B: Condens. Matter **86**, 177 (1992).

[3] B. Dam, J.M. Huijbregtse, F.C. Klaassen, R.C.F. van der Geest, G. Doornbos, J.H. Rector, A.M. Testa, S. Freisem, J.C. Martinez, B. Stäuble-Pümpin, and R. Griessen, Nature (London) **399**, 439 (1999).

[4] R.M. Schalk, K. Kundzins, H.W. Weber, E. Stangl, S. Proyer, and D. Bäuerle, Physica C **257**, 341 (1996).

[5] L. Civale, A.D. Marwick, T.K. Worthington, M.A. Kirk, J.R. Thompson, L. Krusin-Elbaum, J.R. Clem, and F. Holtzberg, Phys. Rev. Lett. **67**, 648 (1991).

[6] V.K. Vlasko-Vlasov, L.A. Dorosinskii, A.A. Polyanskii, V.I. Nikitenko, U. Welp, B.W. Veal, and G.W. Crabtree, Phys. Rev. Lett. **72**, 3246 (1994).

[7] J.N. Li, A.A. Menovsky, and J.J. M. Franse, Phys. Rev. B **48**, 6612 (1993).

[8] R.J. Wijngaarden, R. Griessen, J. Fendrich, and W.-K. Kwok,

Phys. Rev. B **55**, 3268 (1997).
[9] M. Oussena, P.A.J. de Groot, S.J. Porter, R. Gagnon, and L. Taillefer, Phys. Rev. B **51**, 1389 (1995).
[10] T. Haage, J.Q. Li, B. Leibold, M. Cardona, J. Zegenhagen, H.-U. Habermeier, A. Forkl, Ch. Jooss, R. Warthmann, and H. Kronmüller, Solid State Commun. **99**, 553 (1996).
[11] T. Haage, J. Zegenhagen, J.Q. Li, H.-U. Habermeier, M. Cardona, Ch. Jooss, R. Warthmann, A. Forkl, and H. Kronmüller, Phys. Rev. B **56**, 8404 (1997).
[12] Ch. Jooss, R. Warthmann, H. Kronmüller, T. Haage, H.-U. Habermeier, and J. Zegenhagen, Phys. Rev. Lett. **82**, 632 (1999).
[13] A. Diaz, L. Mechin, P. Berghuis, and J.E. Evetts, Phys. Rev. Lett. **80**, 3855 (1998).
[14] D. Dimos, P. Chaudhari, J. Mannhart, and F.K. LeGoues, Phys. Rev. Lett. **61**, 219 (1988).
[15] J. Mannhart and H. Hilgenkamp, Mater. Sci. Eng., B **56**, 77 (1998).
[16] H. Hilgenkamp, J. Mannhart, and B. Mayer, Phys. Rev. B **53**, 14 586 (1996).
[17] A. Gurevich and E.A. Pashitskii, Phys. Rev. B **57**, 13 878 (1998).
[18] N.D. Browning, J.P. Buban, P.D. Nellist, D.P. Norton, M.F. Chisholm, and S.J. Pennycook, Physica C **294**, 183 (1998).
[19] H. Hilgenkamp and J. Mannhart, Appl. Phys. Lett. **73**, 265 (1998).
[20] C.W. Schneider, R.R. Schultz, B. Goetz, A. Schmehl, H. Bielefeldt, H. Hilgenkamp, and J. Mannhart, Appl. Phys. Lett. **75**, 850 (1999).
[21] N.F. Heinig, R.D. Redwing, J.E. Nordman, and D.C. Larbalestier, Phys. Rev. B **60**, 1409 (1999).
[22] E.V. Thuneberg, Cryogenics **29**, 236 (1989); Phys. Rev. Lett. **48**, 1853 (1982).
[23] C.C. Tsuei, J.R. Kirtley, C.C. Chi, Lock See Yu-Jahnes, A. Gupta, T. Shaw, J.Z. Sun, and M.B. Ketchen, Phys. Rev. Lett. **73**, 593 (1994).
[24] M. Franz, C. Kallin, A.J. Berlinsky, and M.I. Salkola, Phys. Rev. B **56**, 7882 (1997).
[25] P.W. Anderson, J. Phys. Chem. Solids **11**, 26 (1959).
[26] M. Franz, C. Kallin, and A.J. Berlinsky, Phys. Rev. B **54**, R6897 (1996).
[27] G.V.M. Williams, E.M. Haines, and J.L. Tallon, Phys. Rev. B **57**, 146 (1998).
[28] P.J. Hirschfeld and N. Goldfeld, Phys. Rev. B **48**, 4219 (1993).
[29] L. Alff, A. Beck, R. Gross, A. Marx, S. Kleefisch, Th. Bauch, H. Sato, M. Naito, and G. Koren, Phys. Rev. B **58**, 11 197 (1998).
[30] M. Friesen and P. Muzikar, Phys. Rev. B **55**, 509 (1997).
[31] J. Brötz, H. Fuess, T. Haage, and J. Zegenhagen, Phys. Rev. B **57**, 3679 (1998).
[32] A. Forkl, T. Dragon, and H. Kronmüller, J. Appl. Phys. **67**, 3047 (1990).
[33] A. Forkl, Phys. Scr. **T49**, 148 (1993).
[34] Ch. Jooss, A. Forkl, R. Warthmann, H.-U. Habermeier, B. Leibold, and H. Kronmüller, Physica C **266**, 235 (1996).
[35] Ch. Jooss, R. Warthmann, A. Forkl, and H. Kronmüller, Physica C **299**, 215 (1998).
[36] A. Forkl and H. Kronmüller, Phys. Rev. B **52**, 16 130 (1995).
[37] Th. Schuster, H. Kuhn, E.H. Brandt, and S. Klaumünzer, Phys. Rev. B **56**, 3413 (1997).
[38] M.V. Indenbom, A. Forkl, B. Ludescher, H. Kronmüller, H.-U. Habermeier, B. Leibold, G. D'Anna, T.W. Li, P.H. Kes, and A.A. Menovsky, Physica C **226**, 325 (1994).
[39] Th. Schuster, H. Kuhn, and M.V. Indenbom, Phys. Rev. B **52**, 15 621 (1995).
[40] Th. Schuster, M.V. Indenbom, H. Kuhn, H. Kronmüller, M. Leghissa, and G. Kreiselmeyer, Phys. Rev. B **50**, 9499 (1994).
[41] Th. Schuster, H. Kuhn, M.V. Indenbom, M. Leghissa, M. Kraus, and M. Konczykowskii, Phys. Rev. B **51**, 16 358 (1995).
[42] E. Cuche, M.V. Indenbom, M.-O. André, P. Richard, W. Benoit, and Th. Wolf, Physica C **256**, 324 (1996).
[43] Ch. Jooss, R. Warthmann, A. Forkl, T. Haage, J. Zegenhagen, H.-U. Habermeier, and H. Kronmüller, Physica C **282-287**, 2311 (1997).
[44] Th. Schuster, M.V. Indenbom, M.R. Koblischka, H. Kuhn, and H. Kronmüller, Phys. Rev. B **49**, 3443 (1994).
[45] R. Warthmann, Ph.D. thesis, University of Stuttgart, Germany, 1999.
[46] A. Gurevich and L.D. Cooley, Phys. Rev. B **50**, 13 563 (1994).
[47] Ch. Jooss and R. Warthmann (unpublished).
[48] J. Clem, J. Low Temp. Phys. **18**, 427 (1975).
[49] D.O. Welch, IEEE Trans. Magn. **21**, 827 (1984).
[50] G. Zerweck, J. Low Temp. Phys. **42**, 1 (1981).
[51] V. Ambegaokar and A. Baratoff, Phys. Rev. Lett. **10**, 486 (1963).
[52] P.G. de Gennes, Rev. Mod. Phys. **36**, 225 (1964).
[53] L.P. Gor'kov, Zh. Éksp. Teor. Fiz. **36**, 1918 (1959) [Sov. Phys. JETP **9**, 1364 (1959)].
[54] P. G. de Gennes, *Superconductivity of Metals and Alloys* (Benjamin, New York, 1966).
[55] H.W. Zandbergen J. van den Berg, and P.H. Kes, Cryogenics **30**, 633 (1990).